

Direct-current-based image reconstruction versus direct-current included or excluded frequency-domain reconstruction in diffuse optical tomography

Guan Xu,¹ Daqing Piao,^{1,*} Charles F. Bunting,¹ and Hamid Dehghani²

¹School of Electrical and Computer Engineering, Oklahoma State University, Stillwater, Oklahoma, USA 74078

²University of Birmingham, Birmingham B15 2TT, UK

*Corresponding author: daqing.piao@okstate.edu

Received 25 September 2009; revised 16 March 2010; accepted 29 March 2010;
posted 8 April 2010 (Doc. ID 117721); published 25 May 2010

We study the level of image artifacts in optical tomography associated with measurement uncertainty under three reconstruction configurations, namely, by using only direct-current (DC), DC-excluded frequency-domain, and DC-included frequency-domain data. Analytic and synthetic studies demonstrate that, at the same level of measurement uncertainty typical to optical tomography, the ratio of the standard deviation of μ_a over μ_a reconstructed by DC only is at least 1.4 times lower than that by frequency-domain methods. The ratio of standard deviations of D (or μ'_s) over D (or μ'_s) reconstructed by DC only are slightly lower than those by frequency-domain methods. Frequency-domain reconstruction including DC generally outperforms that excluding DC, but as the amount of measurements increases, the difference between the two diminishes. Under the condition of *a priori* structural information, the performances of three reconstruction configurations are seemingly equivalent. © 2010 Optical Society of America

OCIS codes: 170.3880, 170.3010, 170.6960, 170.5270.

1. Introduction

Diffuse optical tomography (DOT) based on measurement of near-infrared (NIR) light diffused through thick biological tissue aims to quantify the heterogeneities of NIR-absorbing chromophores and scattering particles [1]. There are generally three categories of DOT measurements: (1) continuous wave (CW), wherein only steady-state or direct-current (DC) detection is carried out, (2) time domain, wherein the attenuation and pulse-width broadening of the excitation light are the measurands [2–5], and (3) frequency domain, which is mathematically the Fourier-transform equivalent of the time-domain method [6–17] but is considerably less complicated in instrumentation. Frequency-domain detection ideally

renders three types of information: the DC attenuation, the modulation intensity change (AC), and the modulation phase shift (PHS). Some frequency-domain DOT works, however, have utilized AC and PHS [6–12,14,15], rather than the complete measurands of DC, AC, and PHS. Excluding the DC in frequency-domain DOT reconstruction implied that the DC information was considered unlikely to improve the outcome of reconstruction when the AC and PHS are available. Such consideration could have been prompted if the DC information had been redundant in frequency-domain reconstruction, but indeed it has not been either justified or negated.

On the other hand, many works in DOT have relied on only the DC measurements [18–26]. Although lacking phase information will certainly reduce the accuracy or confidence of quantitative reconstruction, almost all these studies have demonstrated that the absorption and reduced scattering characteristics can

be separately and absolutely reconstructed by use of DC information only. But all these works lack a direct comparison of the outcome of DC-based reconstruction with that of frequency-domain reconstruction, which is needed to provide a basis to assess the compromise for reconstruction based solely upon DC information. Out of these DC-based DOT reconstructions, there also exists a common but not widely stated feature in the images—the recovered background is usually more homogeneous than the general level of background artifacts seen in images reconstructed in the frequency domain. Fewer image artifacts in the background may be beneficial for identifying the target of interest over a relatively heterogeneous background, but what contributes to fewer image artifacts in the background has not been well understood.

This work studies the level of artifacts associated with measurement uncertainties in three modes of image reconstruction, namely DC, AC + PHS, and DC + AC + PHS. The studies are conducted both analytically and by synthetic measurements, to address why the DC-based reconstruction results in fewer background artifacts and to demonstrate that including DC information in frequency domain generally improves the reconstruction outcome. Clearly, the analysis of this study shall be based upon the propagation of measurement noises to the image. Contributing to the image artifacts are a number of noise sources, among which is an error due to coupling loss, as studied by Schweiger *et al.* [27]. That study treated coupling errors as coupling coefficients appended to the solution space, and demonstrated reconstruction of frequency-domain data contaminated with synthetic coupling errors. Similar studies are necessary to understanding reconstruction with contaminated DC data.

The level of artifacts is a critical indicator of the capability of reliably recovering the optical heterogeneity. Ntziachristos *et al.* [28] demonstrated that the reconstruction of localized lesions deteriorated as a function of background heterogeneity. They also found that increasing the dataset size, specifically the number of detectors used, improves the reconstruction of the lesion structure, but does not remove the artifacts. Those results, performed on frequency-domain synthetic and experimental data, indicate that certain artifacts are inherent to image formation and, thereby, cannot be removed completely. The cause of such artifacts must also be inherent to DC-based reconstruction, wherein the outcome relative to frequency-domain reconstruction is unknown.

The analytic approach of this study is based primarily upon a method introduced by Fantini *et al.* [29] to model the accuracies or, equivalently, the errors associated with a two-distance measurement technique for quantifying the optical properties of a bulk homogeneous medium. Reconstructing optical properties in a homogeneous medium is essentially a process of fitting the slopes of measurements with respect to different source–detector distances, for

which Fantini *et al.* introduced their models of the “relative error” of absorption and reduced scattering coefficients using the intensity exponential factor, the AC exponential factor, and the phase factor between the measurements made at two different source–detector distances. The tomography of optical heterogeneity relies on multiple measurements among spatially resolved sources and detectors, and image reconstruction is a process of optimizing the local optical properties to minimize the difference of model prediction for these source–detector pairs with respect to the measured values. The accuracy of reconstruction is thereby dependent upon the capability of distinguishing the signal variations for a single source–detector pair due to all types of measurement fluctuations, as well as local changes of tissue optical properties, such variations among different source–detector pairs, and mapping such variations to the image space. Hence, the “relative error” initially discussed in [29] equally applies to tomography of optical heterogeneity, because the “relative error” of measurement determines the upper limit of reconstruction accuracy; in other words, it sets the “parameter-recovery-uncertainty level” (PRUL) in the tomography images.

This study analyzes the PRULs of the absorption coefficient, the reduced scattering coefficient, and the diffusion coefficient, for the measurement conditions of DC, AC + PHS, and DC + AC + PHS and examines their representations as image artifacts in synthetic models. Much of the analytic approach of this study is based upon the method established in [29]; however, there are substantial differences in the measurement configurations investigated, and also, in this novel study, the analytic results partially suggested by [29] are quantitatively evaluated to compare the PRULs among these configurations. It is also noted that [29] considered the measurement configurations of DC + AC, AC + PHS, and DC + PHS. When frequency-domain (FD) information is available, it is straightforward to apply AC + PHS, as employed by many works [6–12,14,15], to image reconstruction. The utilization of DC + AC and DC + PHS are mathematically valid; however, those configurations have seldom been used for image reconstruction. This study investigates the level of artifacts in the DC, AC + PHS, and DC + AC + PHS configurations, as they are the most likely implemented approaches toward image reconstruction. Therefore, among the results previously stated in [29], only those related to AC + PHS have been included in this study when appropriate. The AC + PHS result for the absorption coefficient in [29] is cited directly, but the AC + PHS result in [29] for reduced scattering is revised to a more generalized form that is consistent with the result for the absorption coefficient. Table 1 in Subsection 2.A is introduced to make clear these distinctions. This study also investigates reconstruction of the diffusion coefficient, because, not only are the absorption and reduced scattering coefficients coupled, but also generally the diffusion

Table 1. Comparison of the Analytic Derivations in This Work with That in [29]

	Measurements				
	DC	DC + AC	AC + PHS	DC + PHS	DC + AC + PHS
$\frac{\Delta\mu_a}{\mu_a} \left(\frac{\sigma_{\mu_a}}{\mu_a} \right)$	This study	[29]	[29]	[29]	This study
$\frac{\Delta\mu'_s}{\mu'_s} \left(\frac{\sigma_{\mu'_s}}{\mu'_s} \right)$	This study	[29]	[29] ^a	[29]	This study
$\frac{\Delta D}{D} \left(\frac{\sigma_D}{D} \right)$	This study		This study		This study

^aThe derivation was revised to a more generalized form.

coefficient is involved in the reconstruction process *prior* to formulating the reduced scattering coefficient. The diffusion coefficient image may provide new insights to the study even though its artifacts are expected to be close to those seen in reduced scattering image.

The rest of the paper is organized in the following sections. Section 2 analyses the PRUL for three categories: (1) D.C. only, (2) AC + PHS, and (3) DC + AC + PHS. Tissue and measurement parameters typical to optical tomography applications are implemented to evaluate quantitatively the PRULs expected in the images. Section 3 uses synthetic data to examine the uncertainty of the parameters recovered for homogeneous medium, single inclusion with different types of optical contrast, and multiple inclusions with specific optical contrasts. These synthetic models are also evaluated selectively for the condition of having spatial *a priori* information in the image reconstruction. Section 4 discusses the implications of the results.

2. Theory

The reconstruction accuracy of optical tomography is determined by many factors, including the accuracy of the forward model, the determinacy of inverse formulation, and the characteristics of instrument noise [30]. An analytic approach has been introduced in [29] to demonstrate that the uncertainty (or error) in the measurement maps to the uncertainty of recovering the assembled optical properties of bulk tissue. The same uncertainty (or error) of the measurement, when involved in tomographic reconstruction to recover spatially resolved tissue optical properties, will translate to spatially varying artifacts that reduce the contrast-to-noise ratio (CNR) of the target of interest. This effect may seem obvious; however, the extent of it is not well understood. This work closes this gap of knowledge in three conditions of DOT measurements, namely DC, AC + PHS, and complete frequency-domain information by DC + AC + PHS.

A. Parameter-Recovery-Uncertainty Level

The variation of the recovered optical properties is modeled as PRUL, which for AC + PHS has been derived in [29] in terms of the attenuation of the AC amplitude and phase shift versus a change of source–detector distances. We implement the approach in [29], but extend it to DC-only and DC + AC + PHS configurations, and apply it to diffusion

coefficients in addition to absorption and reduced scattering coefficients.

The frequency-domain measurement of photon density consists of a steady state and time-varying components as $U_{FD}(\vec{r}, \omega) = U_{DC}(\vec{r}) + U_{AC}(\vec{r}, \omega)$, where \vec{r} is the position vector and ω is the angular modulation frequency of the light source. The $U_{FD}(\vec{r}, \omega)$ satisfies the photon diffusion equation of

$$\begin{aligned} & \left(-\frac{\mu_a(\vec{r})}{D(\vec{r})} + \frac{i\omega}{vD(\vec{r})} \right) U_{FD}(\vec{r}, \omega) + \nabla^2 U_{FD}(\vec{r}, \omega) \\ & = -\frac{S(\vec{r}, \omega)}{D(\vec{r})}, \end{aligned} \quad (1)$$

where v is the speed of light in the medium, μ_a is the absorption coefficient, $D = [3(\mu_a + \mu'_s)]^{-1}$ is the diffusion coefficient, μ'_s is the reduced scattering coefficient, and the source term $S(\vec{r}, \omega)$ has a DC component $S_{DC}(\vec{r})$ and a time-varying component $S_{AC}(\vec{r}, \omega)$. For a homogeneous infinite medium with a detector at \vec{r} and a source at \vec{r}' , thereby a source–detector distance of $d = |\vec{r}' - \vec{r}|$, we have

$$\begin{aligned} U_{FD}(r, \omega) &= U_{DC}(r) + |U_{AC}(r, \omega)| \exp(i\Phi_{AC}) \\ &= \frac{S_{DC}(r')}{4\pi Dd} \exp(-k_{DC}d) \\ &\quad + \frac{S_{AC}(r', \omega)}{4\pi Dd} \exp(-k_{AC}d) \cdot \exp(ik_{PHS}d), \end{aligned} \quad (2)$$

where

$$\begin{aligned} k_{DC} &= \sqrt{\frac{\mu_a}{D}}, & k_{AC} &= \sqrt{\frac{\mu_a}{2D} \left(\sqrt{1 + \frac{\omega^2}{v^2\mu_a^2}} + 1 \right)}, \\ k_{PHS} &= \sqrt{\frac{\mu_a}{2D} \left(\sqrt{1 + \frac{\omega^2}{v^2\mu_a^2}} - 1 \right)}. \end{aligned} \quad (3)$$

It is noted that $k_{AC} > k_{DC}$ and k_{AC} is correlated with, but not linearly dependent upon, k_{DC} . The attenuation of the DC component of the photon density is thus not equal to or linearly dependent upon that of the AC component, which is an indication that the DC information would not be a duplication of any of AC or PHS.

Denoting $d_2 > d_1$ and $\rho = |d_1 - d_2|$ as the difference of source–detector distance between two mea-

measurements corresponding to the same source, one has [29] (reproduced here for convenience)

$$\begin{aligned} \delta &= \ln\left(\frac{d_2 U_{\text{DC}}(d_2)}{d_1 U_{\text{DC}}(d_1)}\right) = -\rho \cdot k_{\text{DC}} = -\rho \cdot \sqrt{\frac{\mu_a}{D}}, \\ \alpha &= \ln\left(\frac{d_2 U_{\text{AC}}(d_2)}{d_1 U_{\text{AC}}(d_1)}\right) = -\rho \cdot k_{\text{AC}} \\ &= -\rho \cdot \sqrt{\frac{\mu_a}{2D} \left(\sqrt{1 + \frac{\omega^2}{v^2 \mu_a^2}} + 1 \right)}, \\ \phi &= \Phi(d_2) - \Phi(d_1) = \rho \cdot k_{\text{PHS}} \\ &= \rho \cdot \sqrt{\frac{\mu_a}{2D} \left(\sqrt{1 + \frac{\omega^2}{v^2 \mu_a^2}} - 1 \right)}. \end{aligned} \quad (4)$$

Table 1 lists the PRUL of five different measurement configurations, among which three were investigated in [29]. As stated previously, the configuration of DC + AC and DC + PHS were seldom used for image reconstruction, therefore, only the AC + PHS results of [29] are cited for this comparative study.

In CW measurement, we have

$$\mu_a|_{\text{DC}} = D \cdot \left(\frac{\delta}{\rho}\right)^2. \quad (5)$$

References [31,32] suggest that, for steady-state surface measurements, μ_a and D collectively determine the diffuse reflectance, denoted as R_∞ , by the relationship $[\mu_a \cdot D] = K(R_\infty)$. It is noted that the diffuse reflectance is not $U_{\text{DC}}(\vec{r})$, which implies treating $K(R_\infty)$ as not significantly dependent upon $U_{\text{DC}}(\vec{r})$, thereby Eq. (5) may be converted to

$$\mu_a|_{\text{DC}} = \frac{\sqrt{K(R_\infty)}}{\rho} \cdot \delta, \quad (6)$$

and estimating the PRUL of μ_a for DC by

$$\frac{\sigma_{\mu_a}}{\mu_a} \Big|_{\text{DC}} = \frac{1}{\mu_a} \left[\frac{\partial \mu_a}{\partial \delta} \sigma_\delta \right] = \frac{\sigma_\delta}{\delta} \quad \text{or} \quad \left(\frac{\sigma_\delta^2}{\delta^2} \right)^{1/2}. \quad (7)$$

We have, for AC + PHS [29],

$$\mu_a|_{\text{AC+PHS}} = \frac{\omega}{2v} \left(\frac{\phi}{\alpha} - \frac{\alpha}{\phi} \right), \quad (8)$$

and a PRUL of [29]

$$\begin{aligned} \frac{\sigma_{\mu_a}}{\mu_a} \Big|_{\text{AC+PHS}} &= \frac{1}{\mu_a} \left[\left(\frac{\partial \mu_a}{\partial \alpha} \right)^2 \sigma_\alpha^2 + \left(\frac{\partial \mu_a}{\partial \phi} \right)^2 \sigma_\phi^2 \right]^{1/2} \\ &= \frac{\alpha^2 + \phi^2}{\alpha^2 - \phi^2} \left(\frac{\sigma_\alpha^2}{\alpha^2} + \frac{\sigma_\phi^2}{\phi^2} \right)^{1/2}. \end{aligned} \quad (9)$$

For DC + AC + PHS measurement, we have

$$\mu_a|_{\text{DC+AC+PHS}} = -\frac{\omega}{v} \cdot \frac{\delta^2}{2\alpha\phi} \quad (10)$$

and, accordingly, a PRUL of

$$\begin{aligned} \frac{\sigma_{\mu_a}}{\mu_a} \Big|_{\text{DC+AC+PHS}} &= \frac{1}{\mu_a} \left[\left(\frac{\partial \mu_a}{\partial \delta} \right)^2 \sigma_\delta^2 + \left(\frac{\partial \mu_a}{\partial \alpha} \right)^2 \sigma_\alpha^2 + \left(\frac{\partial \mu_a}{\partial \phi} \right)^2 \sigma_\phi^2 \right]^{1/2} \\ &= \left(4 \frac{\sigma_\delta^2}{\delta^2} + \frac{\sigma_\alpha^2}{\alpha^2} + \frac{\sigma_\phi^2}{\phi^2} \right)^{1/2}. \end{aligned} \quad (11)$$

The PRULs in Eqs. (7), (9), and (11) all have the shape of

$$\frac{\sigma_\mu}{\mu} = \eta \cdot (\xi)^{1/2}, \quad (12)$$

which contains a multiplication factor η and a square-root term $\sqrt{\xi}$. The relative levels of these PRULs become comparable as $\frac{\sigma_\phi^2}{\phi^2}$, $\frac{\sigma_\alpha^2}{\alpha^2}$, and $\frac{\sigma_\delta^2}{\delta^2}$ are practically the same [29]. It is indicated in Table 2 that the PRUL of μ_a will be the lowest in DC-based reconstruction, but whether the PRUL of μ_a is lower in AC + PHS or in DC + AC + PHS depends upon the difference in α and ϕ .

Because the image reconstruction recovers D to formulate μ'_a , it is imperative to analyze the PRUL of D . For the case of DC, similar to the derivation for μ_a , we have

$$D|_{\text{DC}} = K(R_\infty) \cdot \left(\frac{\rho}{\delta}\right), \quad (13)$$

Table 2. Comparison on PRUL of μ_a (σ_{μ_a}/μ_a)

Eq.	Condition	η		$\sqrt{\xi}$	
		Expression	Value	Expression	Normalized value
(7)	DC		1	$\left(\frac{\sigma_\delta^2}{\delta^2}\right)^{1/2}$	1
(9)	AC + PHS	$\left(\frac{\alpha^2 + \phi^2}{\alpha^2 - \phi^2}\right)$	>1	$\left(\frac{\sigma_\alpha^2}{\alpha^2} + \frac{\sigma_\phi^2}{\phi^2}\right)^{1/2}$	1.41
(11)	DC + AC + PHS		1	$\left(4 \frac{\sigma_\delta^2}{\delta^2} + \frac{\sigma_\alpha^2}{\alpha^2} + \frac{\sigma_\phi^2}{\phi^2}\right)^{1/2}$	2.45

Table 3. Comparison on PRUL of D

Eq.	Condition	Expression	Normalized Value
(14)	DC	$\left(\frac{\sigma_\delta^2}{\delta^2}\right)^{1/2}$	1
(16)	AC + PHS & DC +AC + PHS	$\left(\frac{\sigma_\alpha^2}{\alpha^2} + \frac{\sigma_\phi^2}{\phi^2}\right)^{1/2}$	~1.41

$$\frac{\sigma_D}{D} \Big|_{DC} = \frac{1}{D} \left[\frac{\partial D}{\partial \delta} \sigma_\delta \right] = \frac{\sigma_\delta}{\delta} \text{ or } \left(\frac{\sigma_\delta^2}{\delta^2} \right)^{1/2}. \quad (14)$$

For AC + PHS and DC + AC + PHS, the expressions are the same:

$$D|_{AC+PHS} = D|_{DC+AC+PHS} = -\frac{\omega \rho^2}{2v} \cdot \frac{1}{\alpha \phi}. \quad (15)$$

Therefore,

$$\begin{aligned} \frac{\sigma_D}{D} |_{AC+PHS} &= \frac{\sigma_D}{D} |_{DC+AC+PHS} \\ &= \frac{1}{D} \left[\left(\frac{\partial D}{\partial \alpha} \right)^2 \sigma_\alpha^2 + \left(\frac{\partial D}{\partial \phi} \right)^2 \sigma_\phi^2 \right]^{1/2} \\ &= \left(\frac{\sigma_\alpha^2}{\alpha^2} + \frac{\sigma_\phi^2}{\phi^2} \right)^{1/2}. \end{aligned} \quad (16)$$

The PRULs of D in Eqs. (14) and (16) are compared in Table 3. Apparently, when AC and phase are employed, the DC component is redundant for the recovery of D .

The PRUL of μ'_s is derived by

$$\begin{aligned} \frac{\sigma_{\mu'_s}}{\mu'_s} &= \frac{1}{\mu'_s} \left[\left(\frac{\partial \mu'_s}{\partial D} \right)^2 \sigma_D^2 + \left(\frac{\partial \mu'_s}{\partial \mu_a} \right)^2 \sigma_{\mu_a}^2 \right]^{1/2} \\ &= \left[\frac{1}{3D} - \mu_a \right]^{-1} \cdot \left[\left(\frac{1}{3D} \right)^2 \left(\frac{\sigma_D}{D} \right)^2 + (\mu_a)^2 \left(\frac{\sigma_{\mu_a}}{\mu_a} \right)^2 \right]^{1/2}, \end{aligned} \quad (17)$$

so the PRUL of μ'_s for DC is

$$\frac{\sigma_{\mu'_s}}{\mu'_s} \Big|_{DC} = \left[\frac{1}{3D} - \mu_a \right]^{-1} \left[\left(\frac{1}{3D} \right)^2 \cdot \left(\frac{\sigma_\delta^2}{\delta^2} \right) + \mu_a^2 \cdot \left(\frac{\sigma_\delta^2}{\delta^2} \right) \right]^{1/2}. \quad (18)$$

For AC + PHS, it is [29,33]

$$\begin{aligned} \frac{\sigma_{\mu'_s}}{\mu'_s} \Big|_{AC+PHS} &= \left[\frac{1}{3D} - \mu_a \right]^{-1} \cdot \left[\left(\frac{1}{3D} \right)^2 \left(\frac{\sigma_\alpha^2}{\alpha^2} + \frac{\sigma_\phi^2}{\phi^2} \right) \right. \\ &\quad \left. + \mu_a^2 \cdot \left(\frac{\alpha^2 + \phi^2}{\alpha^2 - \phi^2} \right)^2 \cdot \left(\frac{\sigma_\alpha^2}{\alpha^2} + \frac{\sigma_\phi^2}{\phi^2} \right) \right]^{1/2}, \end{aligned} \quad (19)$$

and for DC + AC + PHS, it is

$$\begin{aligned} \frac{\sigma_{\mu'_s}}{\mu'_s} \Big|_{DC+AC+PHS} &= \left[\frac{1}{3D} - \mu_a \right]^{-1} \\ &\cdot \left[\left(\frac{1}{3D} \right)^2 \left(\frac{\sigma_\alpha^2}{\alpha^2} + \frac{\sigma_\phi^2}{\phi^2} \right) + \mu_a^2 \right. \\ &\cdot \left. \left(4 \frac{\sigma_\delta^2}{\delta^2} + \frac{\sigma_\alpha^2}{\alpha^2} + \frac{\sigma_\phi^2}{\phi^2} \right) \right]^{1/2}. \end{aligned} \quad (20)$$

Based on the estimation leading to Table 2, the PRULs in Eqs. (19) and (20) can be normalized with respect to Eq. (18). The results are given in Table 4. Again, the PRUL of μ'_s will be the lowest for DC. Whether the PRUL of μ'_s is lower in AC + PHS or in DC + AC + PHS depends also upon the difference in α and ϕ as for the PRUL of μ_a , but, because of the dominance of $1/3D$ over μ_a , the difference between AC + PHS and DC + AC + PHS will be less than that observed for PRUL of μ_a in Table 2.

B. Summary of the PRUL Analyses

The DC-only reconstruction seems to give the least level of relative uncertainty of the parameter in the reconstruction. The AC + PHS configuration seems to be equivalent to DC + AC + PHS in the level of PRULs of reduced scattering and diffusion coefficient, but it is unclear for the absorption coefficient. These analyses have been conducted for an infinite homogeneous medium, but the results will be readily translatable to a medium with boundaries and with inclusions.

3. Synthetic Studies

Simulations are carried out to study the practical issues of PRUL, such as background noise, the accuracy of optical property recovery, and the interparameter cross coupling, of the three measurements setups.

A. Synthetic Model

The forward model is carried out by the finite-element method (FEM) solution of Eq. (1) using the Robin-type boundary condition [34]:

Table 4. Comparison on PRUL of μ'_s

Eq.	Condition	Expression	Normalized as
(18)	DC	$\left[\left(\frac{1}{3D} \right)^2 \left(\frac{\sigma_\delta^2}{\delta^2} \right) + \mu_a^2 \cdot \left(\frac{\sigma_\delta^2}{\delta^2} \right) \right]^{1/2}$	1
(19)	AC + PHS	$\left[\left(\frac{1}{3D} \right)^2 \left(\frac{\sigma_\alpha^2}{\alpha^2} + \frac{\sigma_\phi^2}{\phi^2} \right) + \mu_a^2 \cdot \left(\frac{\alpha^2 + \phi^2}{\alpha^2 - \phi^2} \right)^2 \cdot \left(\frac{\sigma_\alpha^2}{\alpha^2} + \frac{\sigma_\phi^2}{\phi^2} \right) \right]^{1/2}$	>1.41
(20)	DC + AC + PHS	$\left[\left(\frac{1}{3D} \right)^2 \left(\frac{\sigma_\alpha^2}{\alpha^2} + \frac{\sigma_\phi^2}{\phi^2} \right) + \mu_a^2 \cdot \left(4 \frac{\sigma_\delta^2}{\delta^2} + \frac{\sigma_\alpha^2}{\alpha^2} + \frac{\sigma_\phi^2}{\phi^2} \right) \right]^{1/2}$	>1.41

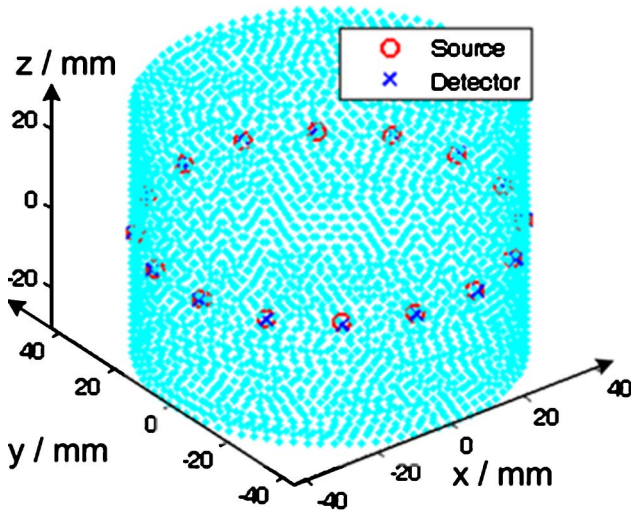


Fig. 1. (Color online) Imaging geometry for a homogeneous medium.

$$U(\vec{r}_0, \omega) - 2DA\hat{n}_0 \cdot \nabla U(\vec{r}_0, \omega) = 0, \quad (21)$$

where A is related to refractive index mismatch and \hat{n}_0 is an outgoing normal vector. The Jacobian is structured to the form of

$$J = \begin{bmatrix} \text{DC} \\ \text{AC} \\ \text{PHS} \end{bmatrix} = \begin{bmatrix} \frac{\partial \ln U_{\text{DC}}}{\partial \mu_a} & \frac{\partial \ln U_{\text{DC}}}{\partial D} \\ \frac{\partial \ln |U_{\text{AC}}|}{\partial \mu_a} & \frac{\partial \ln |U_{\text{AC}}|}{\partial D} \\ \frac{\partial \Phi_{\text{AC}}}{\partial \mu_a} & \frac{\partial \Phi_{\text{AC}}}{\partial D} \end{bmatrix}, \quad (22)$$

where the indices of each block of the Jacobian could be node based for pixelwise reconstruction or region based for *prior*-guided regionwise reconstruction. Utilizing only the first row leads to CW, utilizing the second and third rows renders AC + PHS, and utilizing all three rows gives DC + AC + PHS. The inverse solver implements the Levenberg–Marquardt algorithm as

$$x_{k+1} = x_k + \alpha \cdot [J^T(x_k)J(x_k) + \lambda I]^{-1} J^T(x_k) \Delta v(x_k), \quad (23)$$

where x is the array of unknown parameters, Δv is the forward projection error and λ is a penalty or regularization term. The value of λ is initially set as 100, and is reduced to its fourth root with each continued iteration. The damping factor, α , in the range of (0, 1), is introduced when only regionwise reconstruction is

performed to facilitate stable convergence [35] and is set at 0.5 in this study when included. For pixelwise reconstructions using NIRFAST [36,37], α is set to 1.

B. Simulation Results

Synthetic data are generated for a homogeneous medium, a medium with a single inclusion, and a medium with multiple inclusions with mixed types of optical heterogeneities.

1. PRULs in a Homogeneous Medium

A cylinder-applicator geometry [38] of 60 mm in height and 86 mm in diameter with 16 optodes is adopted, like the one shown in Fig. 1. The optodes are turned on sequentially for the measurements being taken by all other optodes, generating a total of 240 measurements for each dataset.

The volume is discretized into a FEM mesh of 12,695 nodes for forward computation, while a smaller FEM mesh of 600 nodes is used in the reconstruction. Because this synthetic study specifically investigates the level of artifacts reconstructed to the same level of recovered parameters in an otherwise homogeneous medium, the same optical properties of $\mu_a = 0.01 \text{ mm}^{-1}$ and $\mu'_s = 0.01 \text{ mm}^{-1}$ are used for both forward computation and as the initial values of the inverse routine, with 1% noise added to the forward simulation data to maintain the same measurement error. In addition, all controlling parameters of the inverse model are maintained the same for DC, AC + PHS, and DC + AC + PHS configurations.

Table 5 demonstrates that the variations recovered to the parameters of a homogeneous medium are lowest in DC, as expected from the analytic analysis. The DC + AC + PHS slightly outperforms AC + PHS in μ_a recovery, but AC + PHS slightly outperforms DC + AC + PHS in μ'_s/D recovery.

The normalized numbers (1.45–1.64) for μ'_s/D recovery are considerably close to those in the analytical derivation—with the same average optical properties, the background standard deviation of the images reconstructed by FD system measurements is at least 1.41 times larger than those reconstructed by the CW system. However, in μ_a reconstruction, the variations in FD configurations are about twice those predicted in Table 2. It is noted that the analytic results in this study are based upon perturbation analysis. It is well known that DOT is a nonlinear process, wherein the absorption perturbation is more

Table 5. Mean Value and Standard Deviation Reconstructed for Homogeneous Medium

	$\bar{\mu}_a$	$\sigma_{\mu_a} (\text{mm}^{-1})$		$\bar{\mu}'_s$	$\sigma_{\mu'_s} (\text{mm}^{-1})$		\bar{D}	$\sigma_D (\text{mm})$	
		Abs.	Norm.		Abs.	Norm.		Abs.	Norm.
DC	0.01	0.69×10^{-6}	1	1.00	0.80×10^{-4}	1	0.33	2.64×10^{-3}	1
AC + PHS	0.01	3.13×10^{-6}	4.50	1.00	1.18×10^{-4}	1.47	0.33	3.83×10^{-3}	1.45
DC + AC + PHS	0.01	2.98×10^{-6}	4.29	1.00	1.31×10^{-4}	1.64	0.33	4.24×10^{-3}	1.60

^a“Abs.” denotes the absolute value of the standard deviation. “Norm.” denotes the standard deviation normalized with respect to the standard deviation of DC. The same notations apply to Tables 6 and 8.

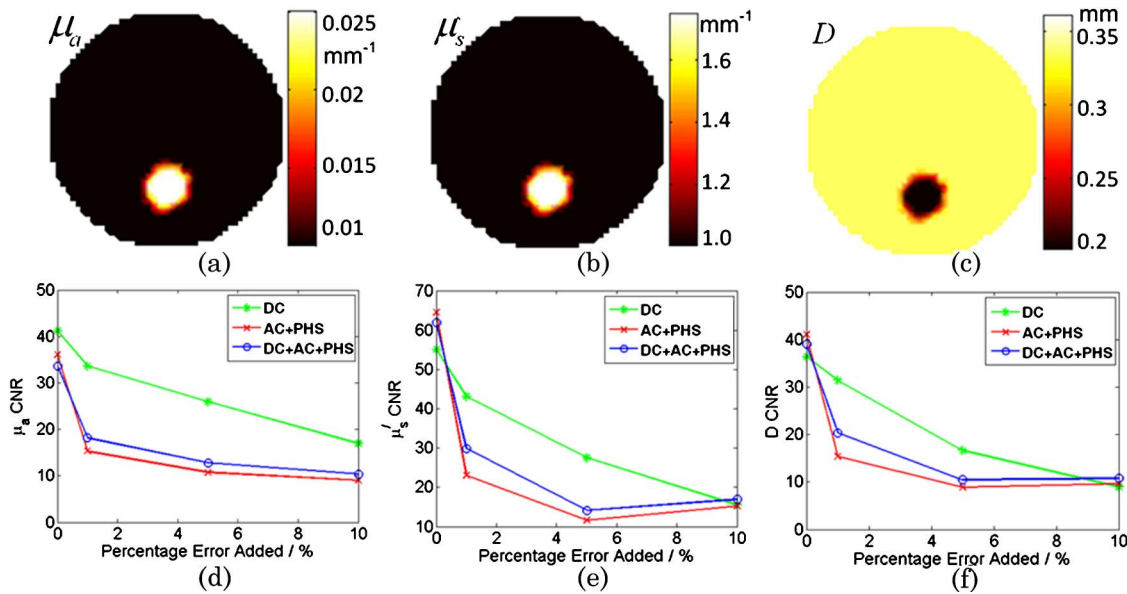


Fig. 2. (Color online) Contrast-to-noise-ratio (CNR) with respect to the measurement noise levels. (a), (b), (c) $\mu_a/\mu'_s/D$ distribution in the $z = 0$ plane of forward model; (d) μ_a CNR comparison; (e) μ'_s CNR comparison; (f) D CNR comparison.

pronounced than scattering perturbation. In this specific model of homogeneous medium, the signal perturbation is evenly distributed to the entire volume of the homogeneous medium instead of mostly confined to smaller lesions with higher optical property contrast, as in the later examinations. Therefore, the perturbations from AC and PHS could have been coupled to and nonlinearly amplified as the variation of absorptions.

2. Contrast-to-Noise Ratio Analysis for Single Target

The results in Subsection 3.B.1 indicate that, for 1% noise in the measurement of homogeneous medium, DC-only reconstruction clearly maintains a lower artifact level compared to DC + AC + PHS and AC + PHS. This study examines the contrast of a target inclusion in an otherwise homogeneous medium

at different measurement noise levels when reconstructed by DC, AC + PHS, and DC + AC + PHS configurations. The synthetic model is similar to that in Subsection 3.B.1, but with a spherical heterogeneity added at $(x = 0 \text{ mm}, y = -20 \text{ mm}, z = 0 \text{ mm})$, with $\mu_a = 0.025 \text{ mm}^{-1}$ and $\mu'_s = 1.75 \text{ mm}^{-1}$. The reconstruction basis of 2760 nodes is larger than the one used for Subsection 3.B.1. Varying noise levels, of 0% to 10%, are integrated into the forward data to examine the CNR of the target ($\text{CNR} = [\max(\text{target-region-value}) - \text{mean}(\text{background-value})] / \text{background-standard-deviation}$) with respect to the background artifacts. The background deviation is calculated by excluding the areas within a distance of 1.5 times the target radius away from its center [39]. The calculated CNRs are given in Fig. 2 for the three types of target contrast. It is observed in Fig. 2 that the CNR levels of μ_a and D look similar when compared to that of μ'_s , which supports the

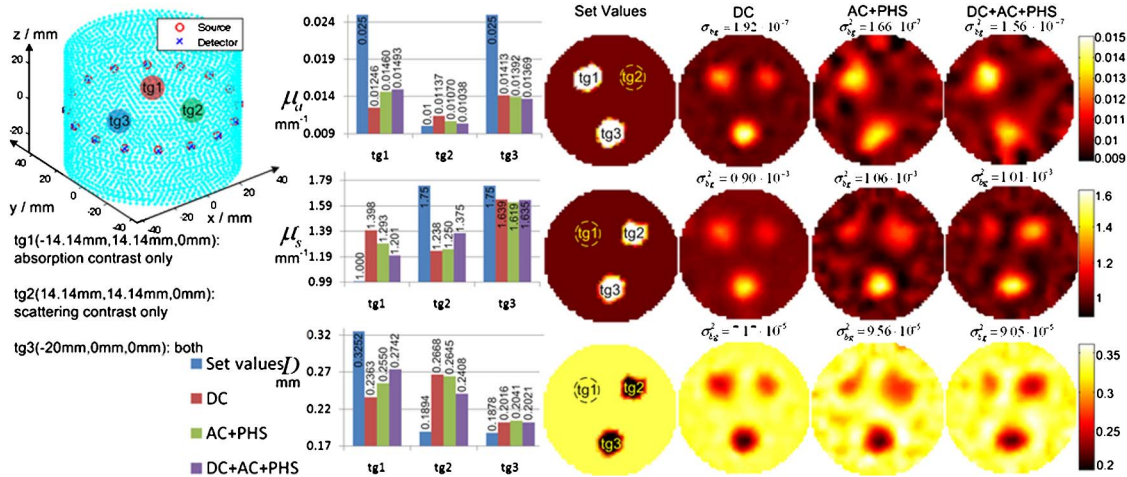


Fig. 3. (Color online) Simulation studies for reconstructing multiple targets in a three-dimensional cylindrical geometry with the optodes and targets located on one plane.

Table 6. Standard Deviation of Background Optical Properties in Fig. 3

	$\sigma_{\mu_a}(\text{mm}^{-1})$		$\sigma_{\mu'_s}(\text{mm}^{-1})$		$\sigma_D(\text{mm})$	
	Abs.	Norm.	Abs.	Norm.	Abs.	Norm.
DC	1.92×10^{-4}	1	2.46×10^{-2}	1	7.25×10^{-3}	1
AC + PHS	3.63×10^{-4}	1.89	2.88×10^{-2}	1.17	9.01×10^{-3}	1.24
DC + AC + PHS	3.45×10^{-4}	1.79	2.49×10^{-2}	1.01	7.75×10^{-3}	1.07

assumptions made for deriving PRULs of μ_a and D in Eqs. (7) and (14). In Fig. 2, the CNR levels of μ_a are found to be lower than that of μ'_s , which may be due to underestimation of μ_a and overestimation of μ'_s in such a pixelwise image reconstruction [24]. Despite this, several features can be observed in Fig. 2. (1) At a zero noise level, the three methods are comparable in the CNR. (2) When the noise becomes higher, the D.C. clearly outperforms the other two in CNR, while DC + AC + PHS slightly outperforms AC + PHS. (3) At a 10% noise level, the CNRs of all methods are similar for μ'_s and D recovery, but DC still outperforms the other two in μ_a reconstruction.

3. Multiple Target Case

The geometry for having multiple inclusions is shown in Fig. 3, where three spherical targets with radii of 7.5 mm are located in the longitudinal middle plane ($z = 0$) of the cylindrical imaging volume and are all 20 mm away from the center of the circular cross section, ensuring the same spatial sensitivity at their positions. Target 1, at the upper left ($x = -14.14$ mm, $y = 14.14$ mm, $z = 0$ mm), has only absorption contrast ($\mu_a = 0.025$ mm⁻¹, $\mu'_s = 1$ mm⁻¹), target 2, at upper right ($x = 14.14$ mm, $y = 14.14$ mm, $z = 0$ mm), has only scattering contrast ($\mu_a = 0.01$ mm⁻¹, $\mu'_s = 1.75$ mm⁻¹), and target 3, at lower side ($x = 0$ mm, $y = -20$ mm, $z = 0$ mm), has contrasts of both absorp-

tion and reduced scattering ($\mu_a = 0.025$ mm⁻¹, $\mu'_s = 1.75$ mm⁻¹). The dashed line in the figure marks the position of the target when it presents no contrast in that category. Table 6 lists the deviation of the background optical property in the reconstructed images. Standard deviation values in Table 6 are normalized along each column versus those of DC-only reconstruction.

For background homogeneity, comparison in Table 6 indicates that DC only demonstrates the lowest artifact level in the image background, while the background artifact levels of DC + AC + PHS and AC + PHS are approximately 1 to 2 times higher. Although the numerical simulative result does not exactly match the values in Tables 2–4, it qualitatively agrees with the analytical derivations. The analytical derivations given in Tables 2–4 indicate that DC + AC + PHS and AC + PHS produce similar background homogeneities, but the simulation results all indicated a slightly lower background artifact level in DC + AC + PHS reconstruction. For target accuracy, the reconstructed images in Fig. 3 and the data comparison in Table 7 are seen with DC + AC + PHS as superior to AC + PHS, which, along with the comparison on the background homogeneity, indicates that including DC generally improves the FD reconstruction. In terms of inter-parameter cross coupling, DC has more coupling than FD, which is well known. The cross coupling

Table 7. Comparison of the Accuracy of Recovered Optical Properties in Fig. 3

	$\mu_{a1}(\text{mm}^{-1})$		$\mu'_{s1}(\text{mm}^{-1})$		$D_1(\text{mm})$	
	Value	Error	Value	Error	Value	Error
Set	0.025		1		0.325	
DC	0.0125	-50.16%	1.398	39.84%	0.236	-27.35%
AC + PHS	0.0146	-41.62%	1.293	29.27%	0.255	-21.59%
DC + AC + PHS	0.0149	-40.30%	1.201	20.06%	0.274	-15.67%
	$\mu_{a2}(\text{mm}^{-1})$		$\mu'_{s2}(\text{mm}^{-1})$		$D_2(\text{mm})$	
	Value	Error	Value	Error	Value	Error
Set	0.01		1.75		1.75	
DC	0.0114	13.68%	1.238	-29.25%	1.639	-6.34%
AC + PHS	0.0107	6.95%	1.250	-28.56%	1.619	-7.47%
DC + AC + PHS	0.0104	3.81%	1.375	-21.45%	1.635	-6.55%
	$\mu_{a3}(\text{mm}^{-1})$		$\mu'_{s3}(\text{mm}^{-1})$		$D_3(\text{mm})$	
	Value	Error	Value	Error	Value	Error
Set	0.025		1.75		0.188	
DC	0.0141	-43.48%	1.639	-6.34%	0.2012	7.37%
AC + PHS	0.0139	-44.31%	1.619	-7.47%	0.204	8.70%
DC + AC + PHS	0.0137	-45.24%	1.635	-6.55%	0.202	7.64%

Table 8. Standard Deviation of Background Optical Properties in Fig. 4

	$\sigma_{\mu_a}(\text{mm}^{-1})$		$\sigma_{\mu_s}(\text{mm}^{-1})$		$\sigma_D(\text{mm})$	
	Abs.	Norm.	Abs.	Norm.	Abs.	Norm.
DC	2.26×10^{-4}	1	3.00×10^{-2}	1	8.47×10^{-3}	1
AC + PHS	4.07×10^{-4}	1.80	3.26×10^{-2}	1.09	9.78×10^{-3}	1.15
DC + AC + PHS	3.95×10^{-4}	1.75	3.18×10^{-2}	1.06	9.51×10^{-3}	1.12

in DC + AC + PHS is slightly less severe than that in AC + PHS.

A similar study is conducted for the same targets in a three-ring setup [38] in Fig. 4, which has three identical rings of optodes at the azimuthal planes of $z = -10 \text{ mm}$, $z = 0 \text{ mm}$, and $z = 10 \text{ mm}$. Each set of data contains a total of 2256 measurements by turning on one source and detecting at all other optodes. The key values are compared in Tables 8 and 9. Most features of the three aspects discussed for the single-ring case can be reconfirmed, except that the target contours recovered by FD reconstructions are more accurately defined, but, nonetheless, the difference between DC + AC + PHS and AC + PHS is insignificant.

Prior-guided region-based reconstructions are also performed on both of the imaging geometries of Figs. 3 and 4 to examine if including accurate *a priori* structural information of the target affects the outcome of the three reconstruction configurations. As is shown in Figs. 5 and 6, with forward models the same as those in Figs. 3 and 4, the inverse model has integrated spatial *a priori* information by assuming a homogeneous target of the accurate size in a homogeneous background. Results of both cases indicate that, with the structural *a priori* information, the performances of the three configurations are essentially equivalent.

4. Discussions

Using only the DC information to simultaneously recover the absorption and diffusion (or the reduced scattering) distributions has been controversial.

The nonuniqueness that may be inherent to DC-only measurements was described in a seminal study [40]. However, despite the negative predictions in [40] that there could be an infinite number of diffusion and absorption pairs leading to the same surface measurements, Harrach [41] proved that, at most, one of them consists of a piecewise constant diffusion and piecewise analytic absorption, and if the true medium has these properties, as in virtually any practical condition, a reconstruction algorithm favoring these properties will pick the right combination of profiles. Harrach's study theoretically justified the experiences in many works that the absorption and scattering distributions have been separately and uniquely recovered by surface measurement of DC only [18–26].

The primary aim of this work is to understand the expectation for DC-based reconstruction in a more systematic approach, thereby establishing a certain level of confidence for the recovered information when only DC information can be relied upon. This work, conveyed by a side-by-side comparison of the reconstructions based on DC, AC + PHS, and DC + AC + PHS, does provide direct evidence that DC-based reconstruction is much less accurate in recovering the absolute optical properties of the target of interest when no additional spatial information is available to confine the reconstruction, as having been universally recognized by the DOT community. However, apart from these well-expected shortcomings, it seems that DC-based reconstruction may not be completely unfavorable. This study generalized the analytical approach initially proposed in [29]

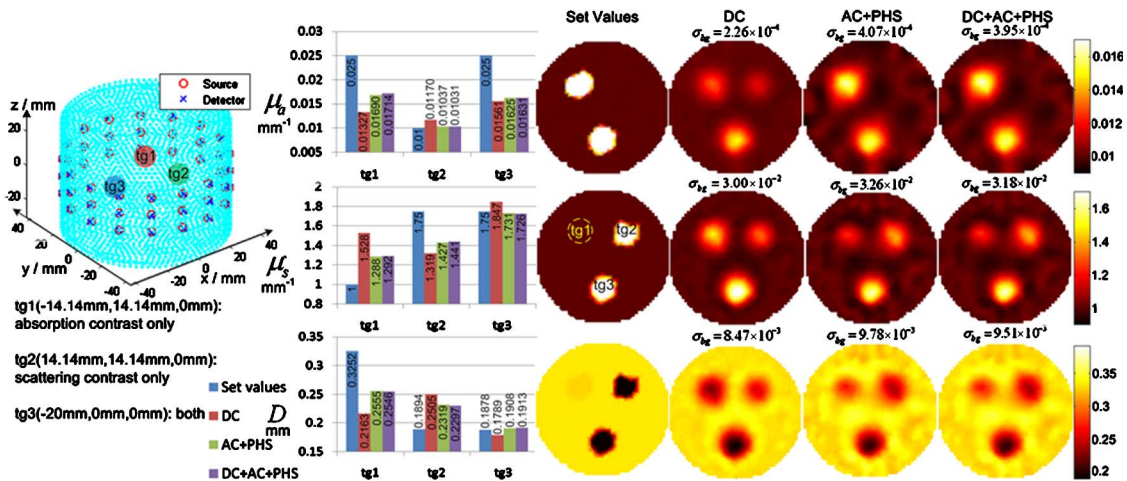


Fig. 4. (Color online) Simulation studies for reconstructing multiple targets in a three-dimensional cylindrical geometry with the optodes located on three different planes and targets located on the middle plane.

Table 9. Comparison of the Accuracy of Recovered Optical Properties in Fig. 4

	$\mu_{a1}(\text{mm}^{-1})$		$\mu'_{s1}(\text{mm}^{-1})$		$D_1(\text{mm})$	
	Value	Error	Value	Error	Value	Error
Set	0.025		1		0.325	
DC	0.0133	-46.93%	1.528	52.81%	0.216	-33.49%
AC + PHS	0.0169	-32.39%	1.288	28.77%	0.256	-21.43%
DC + AC + PHS	0.0171	-31.42%	1.292	29.21%	0.255	-21.70%
	$\mu_{a2}(\text{mm}^{-1})$		$\mu'_{s2}(\text{mm}^{-1})$		$D_2(\text{mm})$	
	Value	Error	Value	Error	Value	Error
Set	0.01		1.75		0.189	
DC	0.0117	16.95%	1.319	-24.63%	0.251	32.26%
AC + PHS	0.0104	3.73%	1.427	-18.45%	0.232	22.46%
DC + AC + PHS	0.0103	3.09%	1.441	-17.66%	0.230	21.31%
	$\mu_{a3}(\text{mm}^{-1})$		$\mu'_{s3}(\text{mm}^{-1})$		$D_3(\text{mm})$	
	Value	Error	Value	Error	Value	Error
Set	0.025		1.75		0.188	
DC	0.0156	-37.57%	1.847	5.57%	0.178	-4.73%
AC + PHS	0.0163	-35.02%	1.731	-1.10%	0.191	1.61%
DC + AC + PHS	0.0163	-34.77%	1.726	-1.38%	0.191	1.88%

to quantify the level of image artifacts that is expressed by the standard deviation of a parameter over the parameter itself. Parameters representative of tissue measurements are used to evaluate the analytic results and conduct the synthetic studies, in both of which the DC reconstruction produced a lower level of relative variation in the optical parameters recovered, and some advantages in the CNR. It may be argued that DC flattens images, leading to a lower standard deviation in the background and, because the background standard deviation is the denominator of CNR, the CNR of DC could become better. But, if there were flattening of the image, then the numerator of the CNR would also be flattened, and perhaps flattened more strongly owing to the nonlinearity of DOT and, thereby, underestimated at a higher level, which collectively might reduce the CNR rather than increase the CNR. The slight but notable CNR advantage of DC-based over FD-based reconstruction demonstrated in this study strongly suggests some inherent advantages of DC, but it could be just because DC has lower information content, similar to what one could expect by reducing the amount of data available or increasing the regularization in FD-based reconstructions.

It is worthwhile to note that this study (as well as most other synthetic studies) assumes a step change of the optical properties of the target of interest with respect to the background. This is not a faithful representation of actual tissue-imaging applications, wherein the target of interest frequently has a tapered or smooth change of contrast over the background. The stronger cross talk between absorption and scattering seen for DC-only reconstruction in this study, as well as many other studies, could have been the outcome of the nonuniqueness, revealed by [40], which is pronounced when the target of interest has a step contrast over the background. In fact, the DC-based reconstruction of *in vivo* measurements has encountered notably different absorption and scattering patterns of a target of interest [42], which may indicate a weaker cross talk for smoother contrast of the target of interest. It is also noted that this study, as well as most other synthetic studies, assumes a globally homogenous yet locally heterogeneous background. An actual tissue environment could be locally homogenous but globally strongly heterogeneous, such as is found in the prostate [26]. In such conditions, a balance or trade-off may exist between the ability of suppressing the background heterogeneity and the likelihood of identifying a

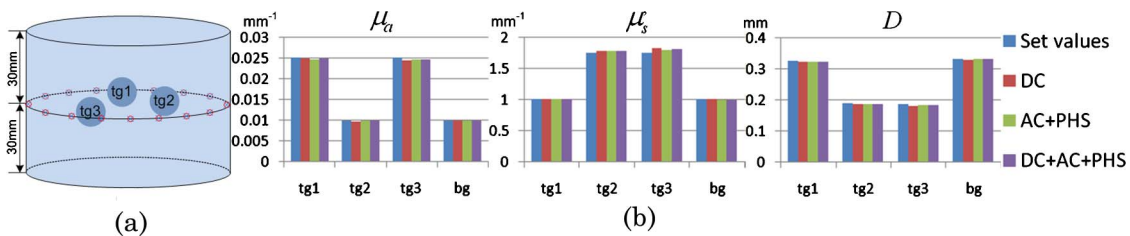


Fig. 5. (Color online) Region-based reconstruction for multiple targets in a three-dimensional cylindrical geometry with the optodes and targets located on one plane. (a) Imaging geometry and the regions of interest; (b) comparison of the results for DC, AC + PHS, and DC + AC + PHS.

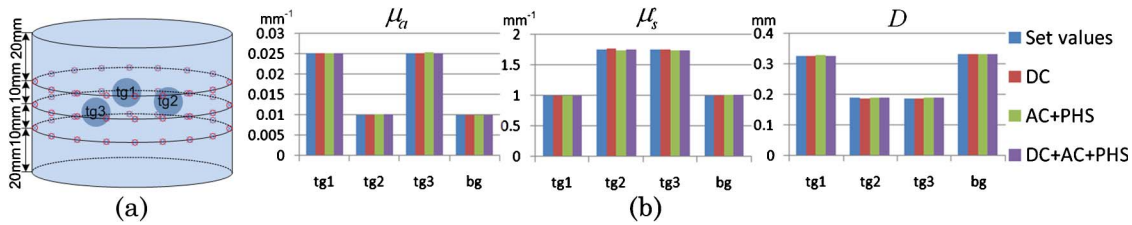


Fig. 6. (Color online) Region-based reconstruction for multiple targets in a three-dimensional cylindrical geometry with the optodes located on three different planes and targets located on the middle plane. (a) Imaging geometry and the regions of interest; (b) comparison of the results for DC, AC + PHS, and DC + AC + PHS.

target of interest in which the contrast is strong locally but weak globally.

This study has also indicated that including DC information in FD reconstruction can sometimes lead to better images than those obtained by ignoring it. The expressions of δ and α in Eq. (4) demonstrate that the DC attenuation is not linearly dependent upon the AC attenuation, and the difference between the two attenuation values increases as the modulation frequency increases. The necessity of including DC in order to optimize the FD reconstruction is made evident by the results in Subsections 3.B.2 and 3.B.3, wherein the DC + AC + PHS results have always been slightly better than the AC + PHS results on the background artifacts, the target properties, and the cross coupling between μ_a and μ'_s/D . However, the slightly better performance of DC + AC + PHS over AC + PHS diminishes as the total number of measurements goes up, as is shown in the three-ring case in Subsection 3.B.3. When fewer measurements are available in application situations, including the DC information in the limited FD measurements likely will improve the overall reconstruction outcome.

This study is carried out for the measurements at a single wavelength. Investigating the PRUL issues in the context of multiband FD measurements will be a natural and more practical extension of this work because most optical tomography measurements are conducted with some kind of spectral information. Besides, similar approaches may be extended to other applications wherein the measurement data contains multiple aspects of information, from which the data usage may be optimized for the specific system configuration.

5. Conclusions

The level of variations of recovered optical properties in optical tomography associated with the measurement uncertainty under three reconstruction configurations of DC-only, the DC-excluded FD, and the DC-included FD is studied by analytic and synthetic means. It is demonstrated that, at the same level of measurement uncertainty typical to optical tomography and under pixelwise reconstruction without spatial *a priori* information, the standard deviations of μ_a over μ_a reconstructed by DC only are at least 1.4 times lower than those obtained by FD methods. The standard deviations of D (or μ'_s) over D (or μ'_s) reconstructed by DC only are slightly lower than those by

FD methods. Frequency-domain reconstruction including DC generally outperforms reconstruction excluding DC, but the difference between the two becomes less significant when the total amount of measurements becomes larger. For FD reconstruction with no spatial *a priori* information and a smaller number of measurements, including DC is recommended. When *a priori* structural information is available, the three reconstruction configurations investigated in this study perform equally well.

This work has been supported in part by the Prostate Cancer Research Program of the U.S. Army Medical Research Acquisition Activity (USAMRAA) through grant W81XWH-07-1-0247, and the Health Research Program of Oklahoma Center for the Advancement of Science and Technology (OCAST) through grant HR06-171. We are grateful to the anonymous reviewers for their constructive comments that enriched the discussions of this work.

References and Notes

1. S. R. Arridge, "Optical tomography in medical imaging," *Inverse Probl.* **15**, R41–R93 (1999).
2. F. Gao, H. Zhao, Y. Tanikawa, and Y. Yamada, "Optical tomographic mapping of cerebral haemodynamics by means of time-domain detection: methodology and phantom validation," *Phys. Med. Biol.* **49**, 1055–1078 (2004).
3. H. Rinneberg, D. Grosenick, K. T. Moesta, J. Mucke, B. Gebauer, C. Stroszczynski, H. Wabnitz, M. Moeller, B. Wassermann, and P. M. Schlag, "Scanning time-domain optical mammography: detection and characterization of breast tumors in vivo," *Technol. Cancer Res. Treat.* **4**, 483–496 (2005).
4. T. Tanifuji and M. Hijikata, "Finite difference time domain (FDTD) analysis of optical pulse responses in biological tissues for spectroscopic diffused optical tomography," *IEEE Trans. Med. Imaging* **21**, 181–184 (2002).
5. W. Mo and N. Chen, "Fast time-domain diffuse optical tomography using pseudorandom bit sequences," *Opt. Express* **16**, 13643–13650 (2008).
6. B. W. Pogue, M. S. Patterson, H. Jiang, and K. D. Paulsen, "Initial assessment of a simple system for frequency domain diffuse optical tomography," *Phys. Med. Biol.* **40**, 1709–1729 (1995).
7. B. W. Pogue, T. O. McBride, J. Prewitt, U. L. Osterberg, and K. D. Paulsen, "Spatially variant regularization improves diffuse optical tomography," *Appl. Opt.* **38**, 2950–2961 (1999).
8. J. Wang, S. Jiang, K. D. Paulsen, and B. W. Pogue, "Broadband frequency-domain near-infrared spectral tomography using a mode-locked Ti:sapphire laser," *Appl. Opt.* **48**, D198–D207 (2009).
9. D. M. Hueber, M. A. Franceschini, H. Y. Ma, Q. Zhang, J. R. Ballesteros, S. Fantini, D. Wallace, V. Ntzachristos,

- and B. Chance, "Non-invasive and quantitative near-infrared hemoglobin spectrometry in the piglet brain during hypoxic stress, using a frequency-domain multidistance instrument," *Phys. Med. Biol.* **46**, 41–62 (2001).
10. M. A. Franceschini, K. T. Moesta, S. Fantini, G. Gaida, E. Gratton, H. Jess, W. W. Mantulin, M. Seeber, P. M. Schlag, and M. Kaschke, "Frequency-domain techniques enhance optical mammography: initial clinical results," *Proc. Natl. Acad. Sci. USA* **94**, 6468–6473 (1997).
 11. N. G. Chen, M. Huang, H. Xia, D. Piao, E. Cronin, and Q. Zhu, "Portable near-infrared diffusive light imager for breast cancer detection," *J. Biomed. Opt.* **9**, 504–510 (2004).
 12. M. J. Holboke, B. J. Tromberg, X. Li, N. Shah, J. Fishkin, D. Kidney, J. Butler, B. Chance, and A. G. Yodh, "Three-dimensional diffuse optical mammography with ultrasound localization in a human subject," *J. Biomed. Opt.* **5**, 237–247 (2000).
 13. B. J. Tromberg, B. W. Pogue, K. D. Paulsen, A. G. Yodh, D. A. Boas, and A. E. Cerussi, "Assessing the future of diffuse optical imaging technologies for breast cancer management," *Med. Phys.* **35**, 2443–2451 (2008).
 14. E. S. Papazoglou, M. S. Weingarten, L. Zubkov, L. Zhu, S. Tyagi, and K. Pourezaci, "Near infrared diffuse optical tomography: improving the quality of care in chronic wounds of patients with diabetes," *Biomed. Instrum. Technol.* **41**, 83–87 (2007).
 15. G. Gulsen, O. Birgul, M. B. Unlu, R. Shafiiha, and O. Nalcioglu, "Combined diffuse optical tomography (DOT) and MRI system for cancer imaging in small animals," *Technol. Cancer Res. Treat.* **5**, 351–363 (2006).
 16. J. P. Culver, R. Choe, M. J. Holboke, L. Zubkov, T. Durduran, A. Slemple, V. Ntziachristos, B. Chance, and A. G. Yodh, "Three-dimensional diffuse optical tomography in the parallel plane transmission geometry: evaluation of a hybrid frequency domain/continuous wave clinical system for breast imaging," *Med. Phys.* **30**, 235–247 (2003).
 17. H. K. Kim, U. J. Netz, J. Beuthan, and A. H. Hielscher, "Optimal source-modulation frequencies for transport-theory-based optical tomography of small-tissue volumes," *Opt. Express* **16**, 18082–18101 (2008).
 18. N. Iftimia and H. Jiang, "Quantitative optical image reconstruction of turbid media by use of direct-current measurements," *Appl. Opt.* **39**, 5256–5261 (2000).
 19. A. M. Siegel, J. J. A. Marota, and D. A. Boas, "Design and evaluation of a continuous-wave diffuse optical tomography system," *Opt. Express* **4**, 287–298 (1999).
 20. Y. Xu, X. Gu, T. Khan, and H. Jiang, "Absorption and scattering images of heterogeneous scattering media can be simultaneously reconstructed by use of dc data," *Appl. Opt.* **41**, 5427–5437 (2002).
 21. Z. Yuan and H. Jiang, "Image reconstruction scheme that combines modified Newton method and efficient initial guess estimation for optical tomography of finger joints," *Appl. Opt.* **46**, 2757–2768 (2007).
 22. H. Jiang, K. D. Paulsen, U. L. Osterberg, and M. S. Patterson, "Improved continuous light diffusion imaging in single- and multi-target tissue-like phantoms," *Phys. Med. Biol.* **43**, 675–693 (1998).
 23. Y. Pei, H. L. Graber, and R. L. Barbour, "Normalized-constraint algorithm for minimizing inter-parameter cross-talk in DC optical tomography," *Opt. Express* **9**, 97–109 (2001).
 24. Z. Jiang, D. Piao, G. Xu, J. W. Ritchey, G. R. Holyoak, K. E. Bartels, C. F. Bunting, G. Slobodov, and J. S. Krasinski, "Trans-rectal ultrasound-coupled near-infrared optical tomography of the prostate Part II: Experimental demonstration," *Opt. Express* **16**, 17505–17520 (2008).
 25. A. H. Hielscher, A. D. Klose, A. K. Scheel, B. Moa-Anderson, M. Backhaus, U. Netz, and J. Beuthan, "Sagittal laser optical tomography for imaging of rheumatoid finger joints," *Phys. Med. Biol.* **49**, 1147–1163 (2004).
 26. K. K. Wang and T. C. Zhu, "Reconstruction of in-vivo optical properties for human prostate using interstitial diffuse optical tomography," *Opt. Express* **17**, 11665–11672 (2009).
 27. M. Schweiger, I. Nissilä, D. A. Boas, and S. R. Arridge, "Image reconstruction in optical tomography in the presence of coupling errors," *Appl. Opt.* **46**, 2743–2756 (2007).
 28. V. Ntziachristos, A. H. Hielscher, A. G. Yodh, and B. Chance, "Diffuse optical tomography of highly heterogeneous media," *IEEE Trans. Med. Imaging* **20**, 470–478 (2001).
 29. S. Fantini, M. A. Franceschini, J. B. Fishkin, B. Barbieriand, and E. Gratton, "Quantitative determination of the absorption spectra of chromophores in strongly scattering media: a light-emitting-diode based technique," *Appl. Opt.* **33**, 5204–5213 (1994).
 30. D. Boas, T. Gaudette, and S. R. Arridge, "Simultaneous imaging and optode calibration with diffuse optical tomography," *Opt. Express* **8**, 263–270 (2001).
 31. S. L. Jacques, "Reflectance spectroscopy with optical fiber devices and transcutaneous bilirubinometers," in *Biomedical Optical Instrumentation and Laser-Assisted Biotechnology*, A. M. Verga Scheggi, S. Martellucci, A. N. Chester, and R. Pratesi, eds. (Kluwer Academic, 1996), pp. 83–94.
 32. F. Fabbri, M. A. Franceschini, and S. Fantini, "Characterization of spatial and temporal variations in the optical properties of tissuelike media with diffuse reflectance imaging," *Appl. Opt.* **42**, 3063–3072 (2003).
 33. The original derivation in [29] for $\sigma_{\mu'_s}/\mu'_s$ has ρ in the equation, which is inconsistent with that obtained for σ_{μ_a}/μ_a . Equation (19) corrected this inconsistency.
 34. B. W. Pogue, S. Geimer, T. O. McBride, S. Jiang, U. L. Osterberg, and K. D. Paulsen, "Three-dimensional simulation of near-infrared diffusion in tissue: boundary condition and geometry analysis for finite-element image reconstruction," *Appl. Opt.* **40**, 588–600 (2001).
 35. G. Xu, D. Piao, C. H. Musgrove, C. F. Bunting, and H. Dehghani, "Trans-rectal ultrasound-coupled near-infrared optical tomography of the prostate, part I: simulation," *Opt. Express* **16**, 17484–17504 (2008).
 36. H. Dehghani, B. W. Pogue, S. Jiang, B. Brooksby, and K. D. Paulsen, "Three-dimensional optical tomography: resolution in small-object imaging," *Appl. Opt.* **42**, 3117–3128 (2003).
 37. H. Dehghani, M. E. Eames, P. K. Yalavarthy, S. C. Davis, S. Srinivasan, C. M. Carpenter, B. W. Pogue, and K. D. Paulsen, "Near infrared optical tomography using NIRFAST: algorithms for numerical model and image reconstruction algorithms," *Commun. Numer. Meth. Eng.* **25**, 711–732 (2009).
 38. P. K. Yalavarthy, H. Dehghani, B. W. Pogue, and K. D. Paulsen, "Critical computational aspects of near infrared circular tomographic imaging: Analysis of measurement number, mesh resolution and reconstruction basis," *Opt. Express* **14**, 6113–6127 (2006).
 39. M. Huang and Q. Zhu, "A dual-mesh optical tomography reconstruction method with depth correction using *a priori* ultrasound information," *Appl. Opt.* **43**, 1654–1662 (2004).
 40. S. R. Arridge and W. R. B. Lionheart, "Nonuniqueness in diffusion-based optical tomography," *Opt. Lett.* **23**, 882–884 (1998).
 41. B. Harrach, "On uniqueness in diffuse optical tomography," *Inverse Probl.* **25**, 055010 (2009).
 42. Z. Jiang, G. R. Holyoak, K. E. Bartels, J. W. Ritchey, G. Xu, C. F. Bunting, G. Slobodov, and D. Piao, "In vivo trans-rectal ultrasound coupled near-infrared optical tomography of a transmissible venereal tumor model in the canine pelvic canal," *J. Biomed. Opt.* **14**, 030506 (2009).